JACS
JOURNAL OF THE AMERICAN CHEMICAL SOCIETY

ARTICLE

pubs.acs.org/JACS

Belt-Shaped π-Systems: Relating Geometry to Electronic Structure in a Six-Porphyrin Nanoring

Johannes K. Sprafke,[†] Dmitry V. Kondratuk,[†] Michael Wykes,[‡] Amber L. Thompson,[†] Markus Hoffmann,[†] Rokas Drevinskas,[§] Wei-Hsin Chen,[Δ] Chaw Keong Yong,[Δ] Joakim Kärnbratt,[⊥] Joseph E. Bullock,[¶] Marc Malfois,[#] Michael R. Wasielewski,[¶] Bo Albinsson,[⊥] Laura M. Herz,[Δ] Donatas Zigmantas,[§] David Beljonne,[*,‡] and Harry L. Anderson[*,†]

[†]Department of Chemistry, University of Oxford, Chemistry Research Laboratory, Mansfield Road, Oxford OX1 3TA, United Kingdom

[‡]Chemistry of Novel Materials, University of Mons, Place du Parc 20, B-7000 Mons, Belgium

[§]Department of Chemical Physics, Lund University, SE-22100 Lund, Sweden

[⊥]Department of Chemistry, Chalmers University of Technology, Kemivägen 3, SE-41296 Göteborg, Sweden

[¶]Department of Chemistry and Argonne−Northwestern Solar Energy Research (ANSER) Center, Northwestern University, Evanston, Illinois 60208-3113, United States

[#]Diamond Light Source Ltd., Harwell Science and Innovation Campus, Didcot OX11 0DE, United Kingdom

[Δ]Clarendon Laboratory, Department of Physics, University of Oxford, Parks Road, Oxford OX1 3PU, United Kingdom

Supporting Information

ABSTRACT: Linear π-conjugated oligomers have been widely investigated, but the behavior of the corresponding cyclic oligomers is poorly understood, despite the recent synthesis of π-conjugated macrocycles such as [*n*]cycloparaphenylenes and cyclo[*n*]thiophenes. Here we present an efficient template-directed synthesis of a π-conjugated butadiyne-linked cyclic porphyrin hexamer directly from the monomer. Small-angle X-ray scattering data show that this nanoring is shape-persistent in solution, even without its template, whereas the linear porphyrin hexamer is relatively flexible. The crystal structure of the nanoring−template complex shows that most of the strain is localized in the acetylenes; the porphyrin units are slightly curved, but the zinc coordination sphere is undistorted. The electrochemistry, absorption, and fluorescence spectra indicate that the HOMO−LUMO gap of the nanoring is less than that of the linear hexamer and less than that of the corresponding polymer. The nanoring exhibits six one-electron reductions and six one-electron oxidations, most of which are well resolved. Ultrafast fluorescence anisotropy measurements show that absorption of light generates an excited state that is delocalized over the whole π-system within a time of less than 0.5 ps. The fluorescence spectrum is amazingly structured and red-shifted. A similar, but less dramatic, red-shift has been reported in the fluorescence spectra of cycloparaphenylenes and was attributed to a high exciton binding energy; however the exciton binding energy of the porphyrin nanoring is similar to those of linear oligomers. Quantum-chemical excited state calculations show that the fluorescence spectrum of the nanoring can be fully explained in terms of vibronic Herzberg−Teller (HT) intensity borrowing.

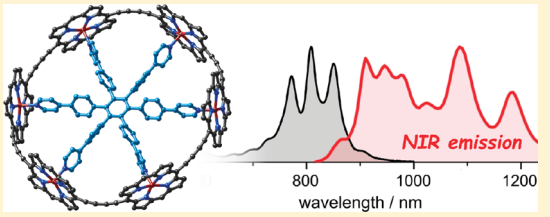

INTRODUCTION

Fully conjugated macrocycles or annulenes are intriguing compounds because they combine an end-free π-system with well-defined size and shape.[1−4] The lack of end-group effects, high symmetry, and the presence of strain can result in surprising changes in the linear and nonlinear optical properties compared with straight-chain oligomers.[1−5] The rigidity of conjugated macrocyles has also been exploited for molecular recognition in solution and on surfaces.[6] Despite the high level of recent interest in π-conjugated nanorings, their synthesis remains challenging. Many approaches rely on statistical oligomerizations, giving mixtures of rings with different sizes, or involve lengthy stepwise synthesis.[1−3,7] The synthesis of belt-like conjugated macrocycles with radially aligned π-orbitals is particularly difficult because these molecules are usually strained.[8] In most cases, as in cyclic *para*-phenylacetylenes[2] or the recently reported cycloparaphenylenes,[3] synthesis of a partially unsaturated cyclic precursor is followed by an efficient reaction that leads to formation of the strained conjugated nanoring. The use of templates can reduce the entropic and enthalpic barrier to cyclization.[4,9,10] We have used this approach to synthesize strained porphyrin nanorings consisting of 6, 8, and 12 porphyrin units.[4] Coordination to the templates not only facilitates the synthesis but also ensures efficient overlap of the

Received: May 19, 2011
Published: September 22, 2011

Scheme 1. Synthesis of Cyclic Hexamer Template Complex *c*-P6·T6 and Free Nanoring *c*-P6[a]

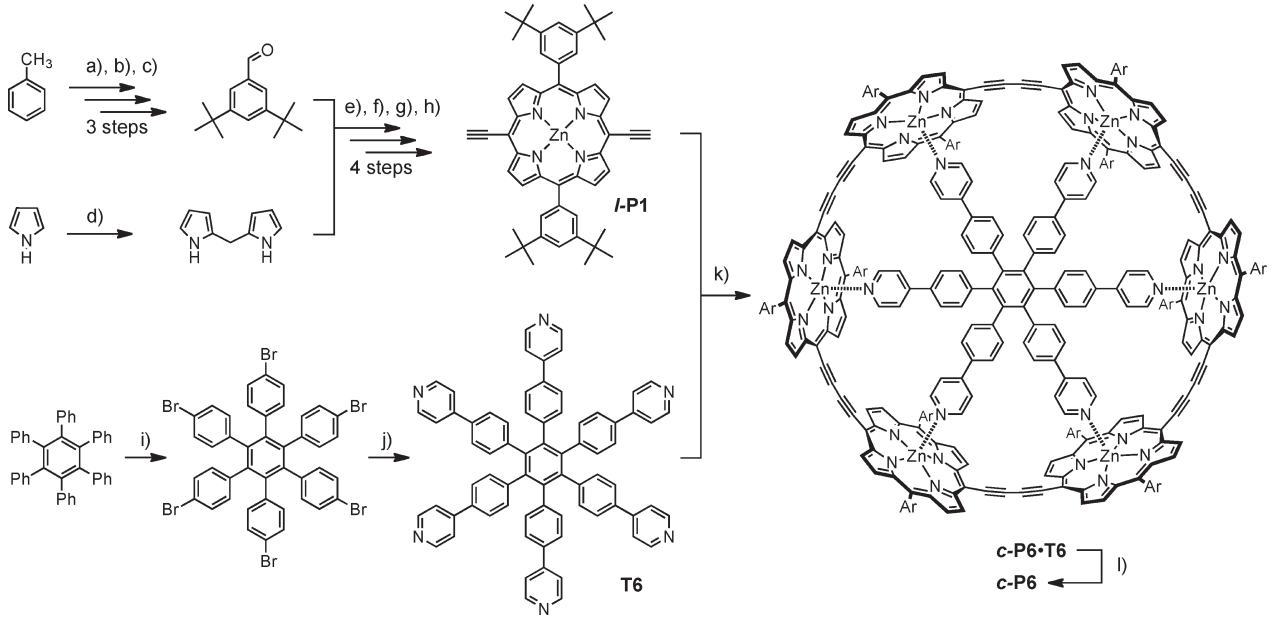

[a] Reaction conditions: (a) *t*-BuCl, $AlCl_3$, 50%;[16a] (b) NBS, $(BzO)_2$;[16a] (c) hexamethylenetetramine, HCl, 64% (over two steps);[16a] (d) CH_2O, TFA, 52%;[16b] (e) TFA then DDQ then $Zn(OAc)_2$, 56%; (f) NBS, 92%; (g) trihexylsilylacetylene, $Pd_2(dba)_3$, CuI, PPh_3, 99%; (h) TBAF, 92%; (i) Br_2, 96%;[4b] (j) 4-pyridineboronic acid, $PdCl_2(PPh_3)_2$, $NaHCO_3$, 50%;[4b,17] (k) $PdCl_2(PPh_3)_2$, CuI, 1,4-benzoquinone, *i*-Pr_2NH, 21%; (l) DABCO, 90%.[4b]

π-orbitals in the final nanoring, by restricting rotation of the individual porphyrin units. This control of conformation should enhance the above-mentioned "ring-effects" and lead to a better understanding of the peculiar electronic properties of fully π-conjugated macrocycles. Furthermore, template binding provides a way of locking a linear oligomer into the curved geometry of a closed nanoring,[11] permitting the effects of conformation to be investigated separately from those of topology.

Here we present an improved template-directed synthesis of the cyclic porphyrin hexamer ***c*-P6**, directly from the porphyrin monomer ***l*-P1** (Scheme 1). Small-angle X-ray scattering data show that this nanoring is shape-persistent in solution, even in the absence of the template. The crystal structure of the nanoring template complex ***c*-P6·T6** indicates that the template is slightly too small for the cavity of the macrocycle, and this conclusion is supported by DFT calculations. The diameter of **T6** is too small for ***c*-P6** by a factor of about 2.5%. The strain energy in the nanoring, compared with the corresponding linear hexamer, is about 101 kJ/mol,[4b] and the crystal structure shows that most of this strain is located in the butadiyne links. The electronic structure of the nanoring was investigated by comparing its electrochemistry and optical spectra with end-capped linear oligomers **Si_2-*l*-P′*N*** and **Bu_2-*l*-P′*N***.[12] The electrochemical and the optical HOMO−LUMO gaps of the nanoring are significantly lower than those of these linear oligomers, and this effect appears to be due to the bending of the π-system. Quantum-chemical excited state calculations at the semiempirical level show that the structured fluorescence spectrum of the nanoring can be fully explained in terms of Herzberg−Teller intensity borrowing from S_2-S_0 to S_1-S_0 transitions. In this respect, ***c*-P6** has a similar electronic structure to benzene. The insights developed here are relevant to understanding the electronic structures of smaller conjugated macrocycles such as cyclothiophenes,[1] cycloparaphenylacetylenes,[2] and cycloparaphenylenes.[3]

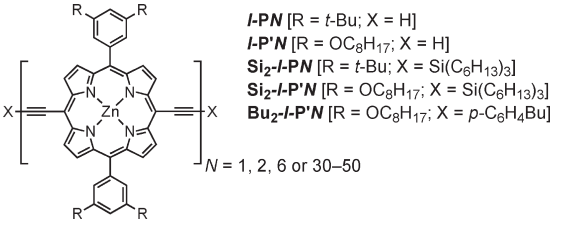

RESULTS AND DISCUSSION

Synthesis. The key step in the synthesis of porphyrin nanoring ***c*-P6** is the oxidative coupling of porphyrin building blocks on a hexadentate template **T6** (Scheme 1). Initially, we used a Pd/Cu cocatalyst system with iodine as the oxidant[13] to couple porphyrin dimer ***l*-P2** on template **T6** at 60 °C, yielding the cyclic hexamer template complex ***c*-P6·T6** in 33−44% yield.[4b] Reaction of porphyrin monomer ***l*-P1** under these conditions gave only a 5% yield of ***c*-P6·T6**. Replacing iodine with 1,4-benzoquinone, as reported by Swager,[14] increased the catalytic activity, enabling the coupling reaction to be carried out at 20 °C and giving ***c*-P6·T6** in 21% yield directly from monomer ***l*-P1**. The increased efficiency of this synthesis probably results from the stronger interaction of the zinc porphyrin units to the template at the lower temperature.[10c] The main byproduct of the cyclization reaction is linear polymer. When using the more active catalyst system (benzoquinone rather than iodine), this polymer is formed with a higher molecular weight, making it more insoluble and easier to remove: After passing the crude reaction mixture over a pad of alumina, the only remaining products are cyclic species that can be readily separated by size exclusion

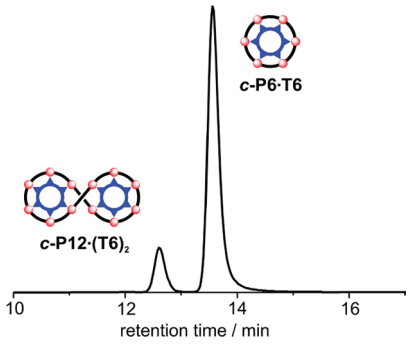

Figure 1. Analytical gel permeation chromatogram of the crude cyclization product eluted in THF (detection wavelength 360 nm). The larger 12-porphyrin figure-of-eight complex ***c*-P12·(T6)$_2$** is eluting first, followed by ***c*-P6·T6**.

chromatography (Figure 1). Besides ***c*-P6·T6**, the recently reported figure-of-eight 12-porphyrin nanoring complex ***c*-P12·(T6)$_2$** is also formed in 4% yield.[4c]

Now that ***c*-P6·T6** can be prepared directly from the porphyrin monomer ***l*-P1**, this nanoring is available in a few steps from simple starting materials as illustrated in Scheme 1. Starting from toluene and pyrrole, 3,5-di(*tert*-butyl)benzaldehyde and dipyrromethane are easily prepared on a multigram scale.[15] Porphyrin synthesis and attachment of terminal acetylenes in the *meso*-positions can be carried out on a gram scale in four steps to give porphyrin monomer ***l*-P1** in an overall yield of 45%.[16] The hexapyridyl template **T6** is accessible in two steps (50% overall yield) via bromination of hexaphenyl benzene followed by a 6-fold Suzuki coupling with 4-pyridineboronic acid.[4b] Addition of a large excess of the competing ligand DABCO (1,4-diazabicyclo[2.2.2]octane) to ***c*-P6·T6** displaces the template to give the free nanoring ***c*-P6** in high yield. The nanoring with solubilizing octyloxy chains in place of the *tert*-butyl groups was prepared under the same reaction conditions in similar yield.[12]

^{1}H NMR Spectroscopy. The high symmetry of the nanoring template complex ***c*-P6·T6** is reflected in its simple ^{1}H NMR spectrum (Figure 2a). The two faces of each porphyrin unit are inequivalent due to the presence of the hexadentate ligand **T6**, resulting in three singlets in the aromatic region, corresponding to the aryl protons c_1, c_2, and *d*, as well as two singlets from *tert*-butyl protons i_1 and i_2. Upon removal of the template, the signals of aryl protons c_1 and c_2 merge into one signal, as do *tert*-butyl protons i_1 and i_2, implying that rotation of the porphyrin units becomes fast on the NMR time scale (Figure 2b).

Solution-Phase Small-Angle X-ray Scattering. SAXS is a well-established technique for solution-phase structure determination of biological macromolecules such as proteins.[17] Over the past few years, it has emerged as an important tool for determining the shapes of large synthetic molecules and molecular assemblies.[4c,18] We found very good agreement between the experimental scattering data and simulated scattering curves calculated from molecular models of ***c*-P6·T6** and ***c*-P6** (Figure 3a,b). The radii of gyration, R_g, determined from a Guinier fit, match the values calculated from models (see Supporting Information). The pair distribution function (PDF) is the normalized probability of finding electron density at separation *r* and can be interpreted more intuitively than the scattering data from which it is obtained by indirect Fourier

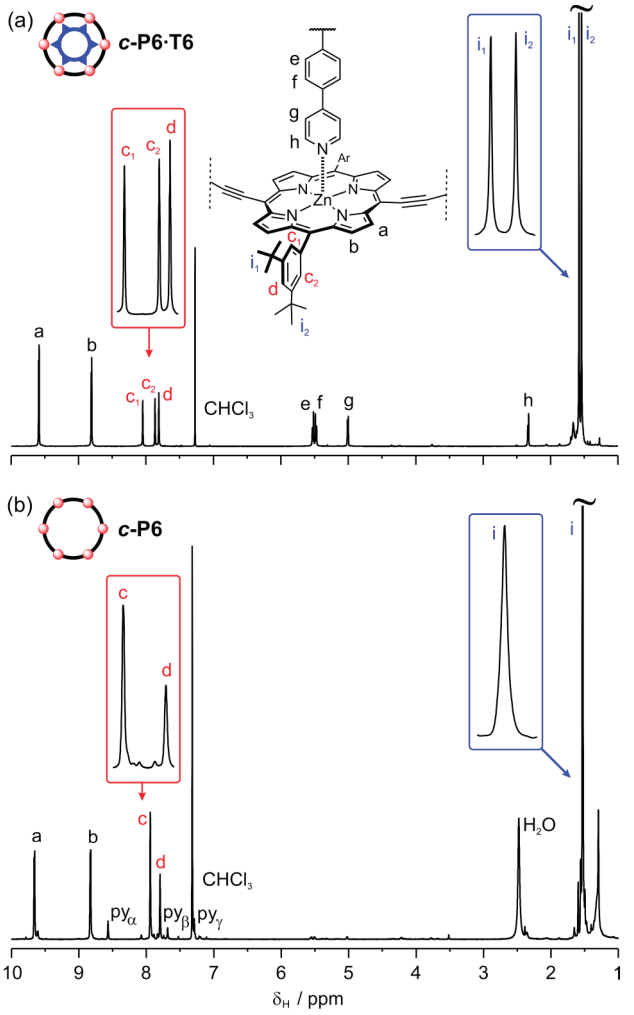

Figure 2. ^{1}H NMR (298 K, 500 MHz) of (a) ***c*-P6·T6** in $CDCl_3$ and (b) ***c*-P6** in $CDCl_3$/1% C_5D_5N.

transformation. PDFs of metalloporphyrin assemblies are particularly informative due to the local point symmetry of the porphyrin cores and the presence of high atomic number metal centers. This often results in well resolved peaks that can be assigned to particular metal−metal distances.[18] The high symmetry of ***c*-P6** and ***c*-P6·T6** results in two distinct peaks that correspond to the distance between two neighboring and two opposite porphyrin units. All features in the PDFs are well reproduced by curves calculated from molecular models. For comparison, Figure 3c shows the scattering data and pair distribution function of linear porphyrin hexamer **Si$_2$-*l*-P′6**. The greater length of this linear oligomer, compared with the cyclic hexamer, is evident from the larger radius of gyration and the presence of peaks at up to 70 Å in the pair distribution function. The five peaks in the PDF correspond to the five distances between porphyrin centers in the hexamer. The shape of the PDF is well reproduced by simulated data from the molecular model; however at increasing distances the model overestimates *r*. This discrepancy is due to the flexibility of **Si$_2$-*l*-P′6** in solution, which reduces the end-to-end length. The excellent agreement between experimental and simulated PDF of ***c*-P6** shows that the shape of the nanoring persists in the absence of the template.

dx.doi.org/10.1021/ja2045919 |*J. Am. Chem. Soc.* 2011, 133, 17262–17273

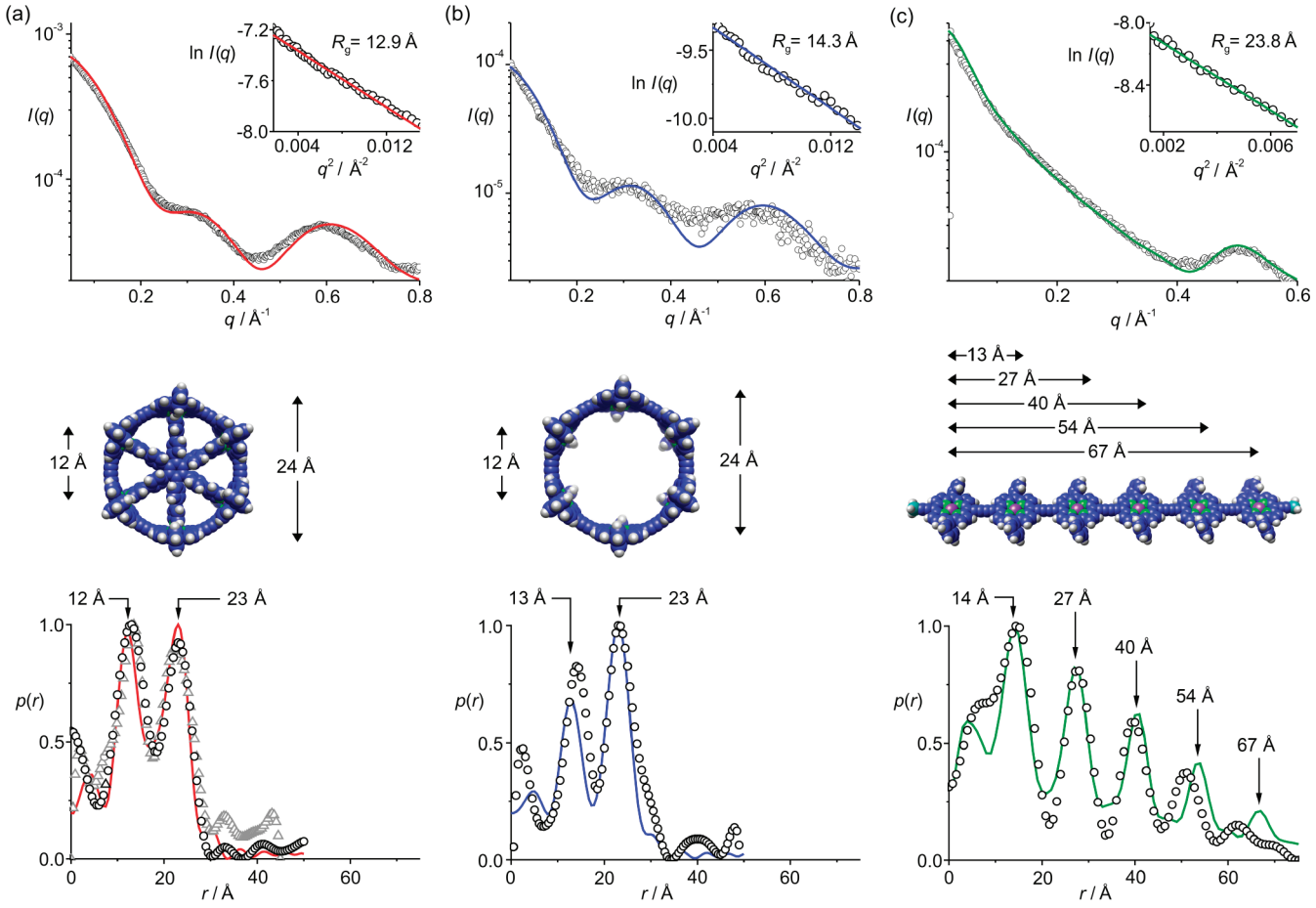

Figure 3. SAXS data for (a) ***c*-P6·T6**, (b) ***c*-P6**, and (c) **Si$_2$-*l*-P′6** acquired in toluene or toluene/1% pyridine at 298 K at the Diamond Light Source, U. K. The top row shows the raw scattering data (black circles) together with the simulated curves based on calculated models (lines). The scattering intensity is a function of the scattering vector, **q**, which is related to the scattering angle 2θ by the relation $\mathbf{q} = (4\pi/\lambda)\sin\theta$, where λ is the X-ray wavelength. The insets are Guinier fits that were used to determine the radii of gyration, R_g. The middle row shows the molecular models that were used to simulate SAXS data, with calculated Zn···Zn distances. Energy minimized structures were obtained using the MM+ force field implemented in the package HyperChem (Hypercube Inc.). The bottom row shows pair distribution functions determined experimentally (black circles) and from models (lines). SAXS data for ***c*-P6·T6** were acquired both at the Diamond Light Source and at the Advanced Photon Source at the Argonne National Laboratory in Chicago, Illinois, USA. The PDF from the data acquired at the Argonne National Laboratory (gray triangles) is in excellent agreement with that from measurements at the Diamond Light Source (black circles).

Crystallography. Determination of the crystal structure of the nanoring was challenging because it forms small weakly diffracting crystals, with large unit cells and substantial amounts of disordered solvent. It is near the upper limit of the size range of synthetic molecules that have been characterized crystallographically, and the Cambridge Structural Database (CSD, version 5.32) contains only two previous structures of covalent porphyrin oligomers with more than five porphyrin units.[19] Crystals of ***c*-P6·T6** were grown by vapor diffusion of *n*-hexane into a solution of ***c*-P6·T6** in $CHCl_3$/1% pyridine. The asymmetric unit contains half a molecule of ***c*-P6·T6**, with a crystallographic inversion center at the center of the molecule. The molecules pack in a herringbone arrangement and form infinite layers (Figure 4a). The experimental mean transannular Zn···Zn distance (24.35 ± 0.08 Å) is in excellent agreement with the previously published calculated value of 24.2 Å.[4b] Molecules of ***c*-P6·T6** are slightly distorted from ideal D_{6h} symmetry, and the nanoring adopts a "chair-like" conformation, with alternate butadiyne links above and below the mean plane of the six zinc atoms (mean deviations of 0.80 Å at C_α and 0.89 Å at C_β, Figure 4b,c). This distortion makes the ***c*-P6** ring contract slightly round the **T6** template, and it reveals that the template is too small for the cavity of the nanoring. However the zinc coordination geometry is essentially normal. The mean zinc to pyridine nitrogen bond length (d_{Zn-Py} = 2.15 ± 0.02 Å) in ***c*-P6·T6** is the same as that reported in the crystal structure of the linear dimer **Si$_2$-*l*-P2** (2.164 ± 0.002 Å)[20] and in other five-coordinate Zn-porphyrin pyridine complexes (Figure 5a; mean value from the CSD, d_{Zn-Py} = 2.16 ± 0.03 Å). The porphyrin units in ***c*-P6·T6** are almost planar: the root-mean-squared deviation for the 24 atoms of the porphyrin core, averaged over all three crystallographically inequivalent porphyrin units, is 0.020 Å, which is less than in the linear dimer **Si$_2$-*l*-P2** (0.043 Å). The porphyrin units are slightly curved around the nanoring, which reduces the distance from the zinc atom to the mean plane of the 24-atom porphyrin core (Figure 5b, $d_{Zn-Porph}$ = 0.24 ± 0.06 Å; mean value from the CSD, $d_{Zn-Porph}$ = 0.37 ± 0.06 Å; in **Si$_2$-*l*-P2**, $d_{Zn-Porph}$ = 0.32 Å). The curvature in the porphyrins is most clearly revealed by the angles between *meso* carbon atoms C(5) and C(15) and the centroid of four pyrrole nitrogens (mean γ = 174.2° ± 0.9°), which is less than the

dx.doi.org/10.1021/ja2045919 |*J. Am. Chem. Soc.* 2011, 133, 17262–17273

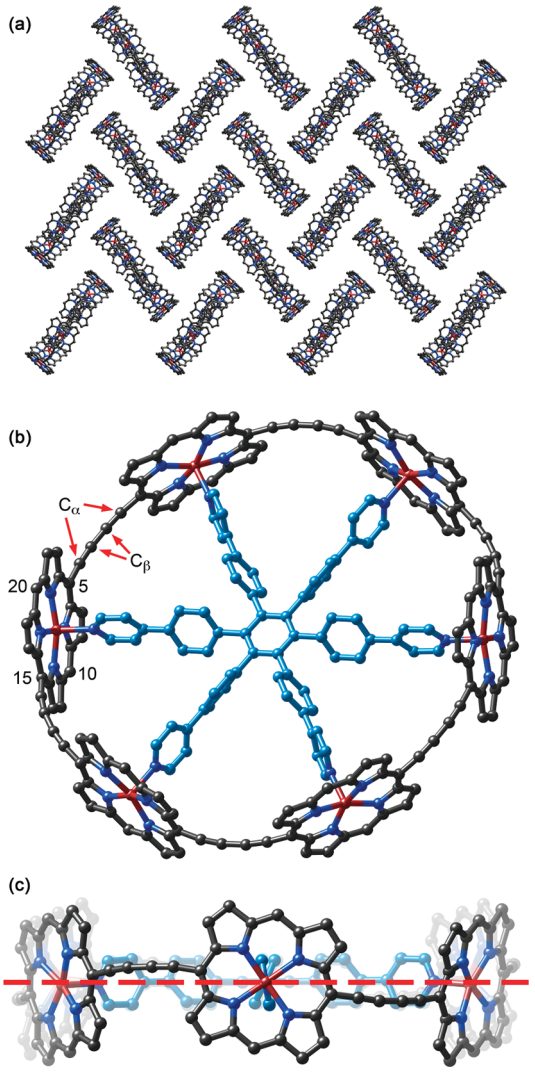

Figure 4. (a) Packing diagram for ***c*-P6·T6**. Front (b) and side (c) views of individual molecules of ***c*-P6·T6** in the crystal with mean plane fitted through six zinc-centers (red dashed line). Hydrogen atoms, aryl groups, and solvent molecules are omitted for clarity.

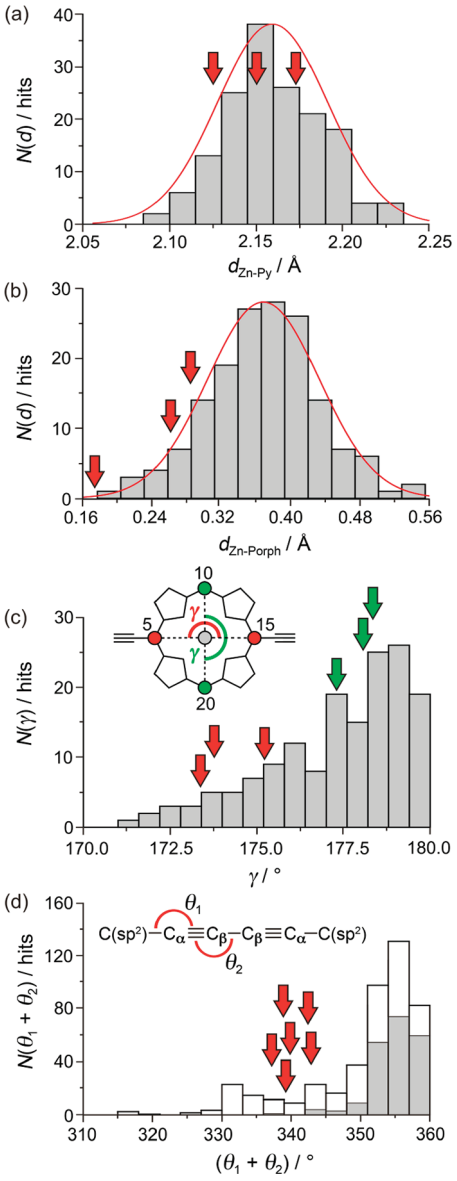

Figure 5. Comparison of crystallographic parameters in ***c*-P6·T6** with those of structural fragments from the Cambridge Crystallographic Database: (a) Zn–N bond length d_{Zn-Py} of the pyridyl nitrogen; (b) out-of-plane distance $d_{Zn-plane}$ of the Zn atom from the plane of the 24-atom porphyrin core; (c) angle between opposite *meso*-positions and centroid of four pyrrole nitrogens γ; (d) sum of the angles C-(sp^2)–C_α≡C_β (θ_1) and C_α≡C_β–C_β (θ_2), compared with acyclic (gray bars) and cyclic (white bars) 1,3-butadiynes. Red and green arrows indicate the values of $d_{Zn-plane}$, d_{Zn-Py}, γ, and (θ_1 + θ_2) over the three inequivalent butadiyne and porphyrin units in ***c*-P6·T6**.

corresponding angle between *meso* carbon atoms C(10) and C(20) (mean γ = 177.9° ± 0.5°; Figure 5c). A similar curved distortion is evident in the porphyrin tetramer nanobarrel reported recently by Osuka and co-workers.[21] Most of the strain in ***c*-P6·T6** is distributed among the acetylenes. The averages of the C(sp^2)–C_α≡C_β and C_α≡C_β–C_β bond angles for the six nonequivalent C≡C units in ***c*-P6·T6** deviate significantly from values found for linear butadiynes in the CSD (Figure 5d). However the distortion in these acetylenes is less than that found in many other butadiyne-linked macrocycles.[22] The average crystallographic C_β–C_β and C_α≡C_β bond lengths in ***c*-P6·T6** are 1.386 ± 0.022 Å and 1.223 ± 0.016 Å, respectively, reflecting a normal level of bond length alternation for a 1,3-butadiyne, in contrast to the behavior observed in longer polyynes.[23]

Electrochemistry. Cyclic and square-wave (SW) voltammetry were carried out on ***c*-P6·T6** and ***c*-P6** in THF in the presence of NBu_4PF_6 (0.10 M). The SW voltammograms are plotted in Figure 6a, for the range −2.2 to +0.8 V (relative to internal ferrocene Fc/Fc^+). The trace for ***c*-P6·T6** appears to show six one-electron reductions and six one-electron oxidations, although the first and second reductions potentials are unresolved, as are the 1st/2nd and 5th/6th oxidations.

In Figure 6b, the first and sixth oxidation and reduction potentials of ***c*-P6·T6** and ***c*-P6** (E^1_{Ox}, E^6_{Ox}, E^1_{Red}, E^6_{Red}) are compared with the first and *N*th oxidation and reduction potentials of **Bu_2-*l*-P′*N***, which vary linearly with 1/*N* (where *N* = 1, 2 and 4; data from ref 24). The HOMO–LUMO gap of ***c*-P6·T6** ($E_g = E^1_{ox} - E^1_{red}$ = 1.55 V) is smaller than the gap extrapolated for an infinite polymer (1.71 eV). The splittings

dx.doi.org/10.1021/ja2045919 |*J. Am. Chem. Soc.* 2011, 133, 17262–17273

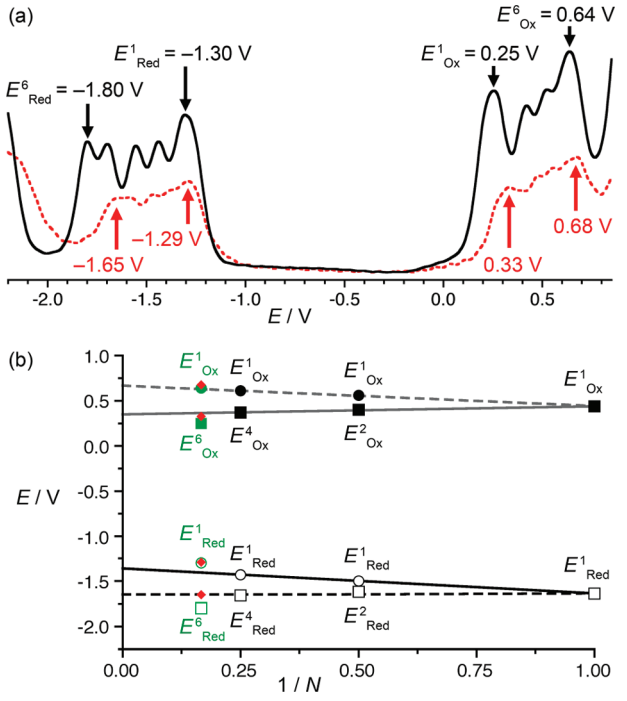

Figure 6. (a) Square-wave voltammograms of ***c*-P6·T6** (black line) and ***c*-P6** (red dashed line) in THF in the presence of NBu_4PF_6 (0.10 M) referenced to internal ferrocene (Fc/Fc^+ at 0.00 V). (b) Comparison of the oxidation and reduction potentials of ***c*-P6·T6** (green points) and ***c*-P6** (red points) with those of **Bu$_2$-*l*-P′*N***, measured under the same conditions.[24]

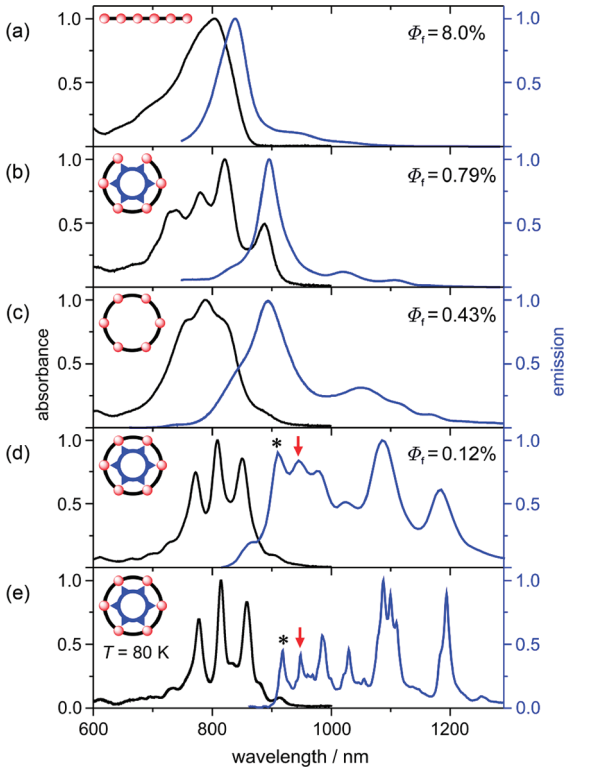

Figure 7. Normalized steady-state absorption (black lines) and fluorescence (blue lines) spectra at 295 K of (a) **Si$_2$-*l*-P′6** in toluene/1% pyridine, (b) **Si$_2$-*l*-P′6·T6** in toluene, (c) ***c*-P6** in toluene/1% pyridine, (d) ***c*-P6·T6** in toluene, and (e) ***c*-P6·T6** in methylcyclohexane at 80 K. Samples were excited at 489 nm, except ***c*-P6·T6** (λ_{ex} = 809 nm at 295 K; λ_{ex} = 856 nm at 80 K). The red arrow indicates the S_1-S_0 0−0 transition at 946 nm and ∗ indicates a fluorescent impurity at 930 nm (see Supporting Information).[25]

between the first and sixth oxidation and reduction potentials of ***c*-P6·T6** ($E^1_{Ox} - E^6_{Ox}$ = 0.39 V; $E^1_{Red} - E^6_{Red}$ = 0.50) are also wider than the extrapolated splittings for the infinite polymer (0.31 and 0.29 V, respectively). Both these comparisons indicate that the electronic coupling in the nanoring is stronger than in the linear oligomers. Removal of the template reduces the resolution between the different redox processes and increases the HOMO−LUMO gap to 1.62 V, but this is still less than the gap expected for an infinite polymer. Thus the strong electronic coupling in ***c*-P6·T6** seems to be partly a consequence of the rigid geometry enforced by the template and partly a consequence of distortion of the π-system. Electrochemical measurements on cyclo[10]thiophene[1b] and [8]cycloparaphenylene[3d] revealed similar strain-induced decreases in the first oxidation potentials, although reduction potentials were not reported for either of these systems, so it is not known whether strain also reduces the electrochemical HOMO−LUMO gap in other π-conjugated macrocycles.

Optical Spectroscopy and Photophysics. The absorption and fluorescence spectra of the linear and cyclic hexamers (**Si$_2$-*l*-P′6** and **P6**) are compared in the presence and absence of the **T6** template in Figure 7.[25] In agreement with the trend seen in the electrochemical HOMO−LUMO gaps, both the onset of absorption and the first emission maxima in ***c*-P6** and ***c*-P6·T6** are red-shifted by 60−70 nm (ca. 0.1 eV) compared with **Si$_2$-*l*-P′6**. A similar effect is observed in the loop complex **Si$_2$-*l*-P′6·T6**. The red shift in the absorption spectra of ***c*-P6·T6** and **Si$_2$-*l*-P′6·T6** may be partly a consequence of the small porphyrin−porphyrin torsional angles in these systems, whereas the full range of torsional angles is populated in **Si$_2$-*l*-P′6**. However when the porphyrin−porphyrin torsional angles are fixed by self-assembly of double-strand ladder complexes (e.g., **(Si$_2$-*l*-P′6)$_2$·(Bipy)$_6$**, see Supporting Information),[16a] this does not result in such a large red-shift, so part of the effect must originate from the curvature of the π-system. Bending the π-system also results in new emission bands at long wavelengths (1000−1300 nm, Figure 7). The relative intensity of these NIR bands increases in the order **Si$_2$-*l*-P′6·T6** < ***c*-P6** < ***c*-P6·T6**, which correlates with the growing rigidity of the porphyrin oligomers. The most rigid species, ***c*-P6·T6**, shows a complex pattern of emission peaks extending to 1300 nm. The appearance of these low-energy NIR bands is accompanied by a dramatic drop in the fluorescence quantum yields (Figure 7), and this effect is most pronounced in the ***c*-P6·T6** complex. The structured absorption and fluorescence spectra of ***c*-P6·T6** become well resolved at low temperatures (e.g., 80 K, Figure 7e). The assignment of these transitions is discussed below.

The fluorescence decay times of ***c*-P6·T6** and **Si$_2$-*l*-P′6** are 250 and 650 ps, respectively.[26] When combined with the fluorescence quantum yields in Figure 7, these data give radiative rate constants of $k_F = 4.8 \times 10^6\ s^{-1}$ for ***c*-P6·T6** and $k_F = 1.2 \times 10^8\ s^{-1}$ for **Si$_2$-*l*-P′6**. The small S_1-S_0 radiative rate constant for ***c*-P6·T6** indicates that its S_1 state is delocalized over all six porphyrin units, as discussed in the next section. Time-resolved fluorescence polarization anisotropy measurements confirmed that optical excitation results in an excited state that is delocalized over the whole nanoring. The initial anisotropies for ***c*-P6** and ***c*-**

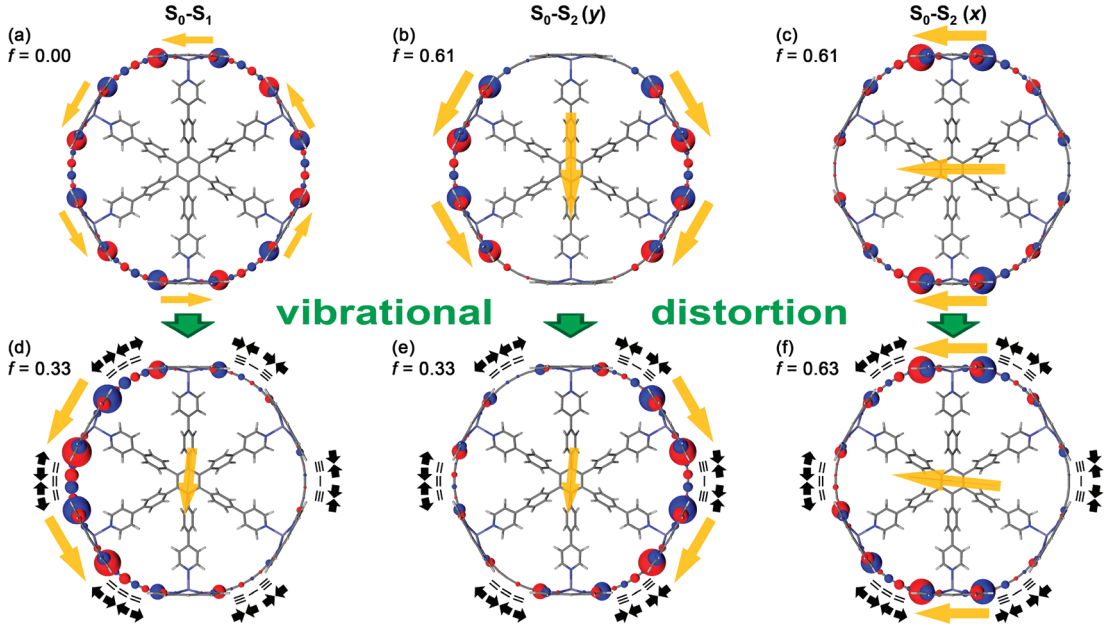

Figure 8. INDO/SCI atomic transition densities (blue and red spheres) and schematic excitonic models of S_1 (a, d) and the *y*-polarized (b, e) and *x*-polarized (c, f) components of the doubly degenerate S_2 at the D_6 symmetric ground state geometry (a−c) and distorted 0.1 a_0 along vibrational mode 968 (d−f). Peripheral yellow arrows indicate the direction of individual porphyrin transition dipole moments, while central yellow arrows show the net transition dipole moments. The black arrows in parts d−f indicate the displacement of butadiyne carbons along mode 968 and bonds inset indicate the direction of the change in bond length alternation.

P6·T6 were found to be 0.08 ± 0.02 and 0.08 ± 0.01, respectively; in both cases, the value remained constant over the period 0.5−20 ps after excitation (see Supporting Information). These anisotropies match the value of 0.1 expected for depolarization over a two-dimensional chromophore. In contrast, the initial fluorescence anisotropy of the linear hexamer **Si$_2$-*l*-P′6** is 0.32 ± 0.02, which is close to the value of 0.4 expected for a linear chromophore.[27] The observation that the anisotropy of **Si$_2$-*l*-P′6** is slightly less than 0.4 reflects the flexibility of this molecule in solution (as indicated by the SAXS data, Figure 3c). These results are consistent with the ultrafast fluorescence depolarization previously reported for the linear octamer **Si$_2$-*l*-P′8** locked into a cyclic conformation by binding to an octapyridyl template.[27]

Theory. The absorption and emission behavior of conjugated macrocycles can be explained in terms of a simple exciton model.[4b,28] In the lowest energy (S_0−S_1) transition of a linear π-system consisting of several component chromophores, the individual transition dipoles of the component chromophores add up to give a strong overall transition dipole. However in the lowest energy transition of the corresponding cyclic oligomer, the individual transition dipoles cancel, leading to no overall transition dipole. Consequently the absorption spectrum of the nanoring is dominated by the strongly allowed S_0−S_2 transition, and emission from S_1 is slow and inefficient, explaining the low fluorescence quantum yield and small radiative rate constant of ***c*-P6·T6**. The cancellation of the transition dipoles is expected to be less complete in more flexible and less symmetrical systems such as **Si$_2$-*l*-P6·T6** and ***c*-P6**, which explains why they fluoresce more efficiently than ***c*-P6·T6**.

Quantum-chemical excited state calculations at the semiempirical intermediate neglect of differential overlap single configuration interaction (INDO/SCI)[29] and time-dependent density functional theory (TD-DFT)[30] levels of theory provide a more detailed picture than this excitonic model. The ground state geometries of ***c*-P6·T6** and ***c*-P6** were optimized (without solubilizing aryl groups and constrained to minimum D_6 symmetry) at the DFT level of theory.[31] While ***c*-P6** was found to exhibit D_{6h} symmetry, the propeller twist of the **T6** template reduced the symmetry of ***c*-P6·T6** to D_6. The lowest singlet excited state S_1 (Figure 8a) has A_{2g} symmetry in ***c*-P6** and A_2 symmetry in ***c*-P6·T6**. In ***c*-P6**, transition between S_0 (A_{1g}) and S_1 (A_{2g}) is forbidden,[32a] while in ***c*-P6·T6** transitions are formally allowed via the $a_2(z)$ component of the electric dipole operator but have a vanishingly small transition dipole moment. However S_0−S_2 transitions are strongly allowed[32b] and doubly degenerate with *x*- and *y*-polarizations (see Figure 8b,c).

In order to develop an interpretation of the low-energy emission bands, it is instructive to compare ***c*-P6** to benzene, with which it shares the same symmetry point group. In benzene, the transitions between the ground state S_0 (A_{1g}) and lowest singlet S_1 (B_{2u}) at approximately 5 eV[33] are forbidden.[32c] The weak absorption band in this spectral region is well studied[34] and interpreted in terms of Herzberg−Teller (HT) intensity borrowing[35] mediated via vibronic coupling. Simulated spectra of benzene including HT coupling have been performed at a very high level of theory and are in excellent agreement with experimental spectra.[36a] Here we calculate the HT emission spectra of ***c*-P6·T6** using more approximate models practical for a system of this size. The physical basis of the HT coupling can be pictured in two equally valid ways: In the first, the nuclear and electronic wave functions are regarded to be completely decoupled at zeroth-order, while perturbative interactions between the S_1 electronic wave function (A_2) and nuclear motions of the correct symmetry (e_1) result in a combined electronic and vibronic state of E_1 symmetry, which can mix with nearby purely electronic states of the same E_1 symmetry. Because electric dipole transitions from E_1 to A_1 are strongly allowed,[32d] the mixing results in

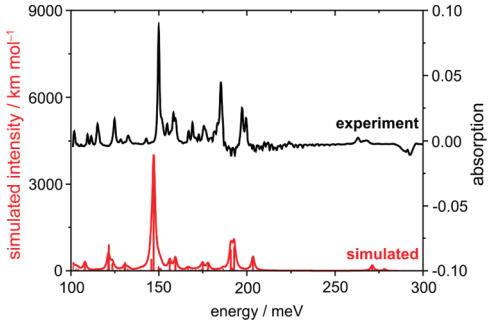

Figure 9. Infrared spectra of ***c*-P6·T6**: experimental spectrum in CCl_4 (black line), DFT stick spectrum (red bars, frequencies have been scaled by 0.94), and DFT convoluted spectrum (red line, Lorentzian γ = 0.01 eV).

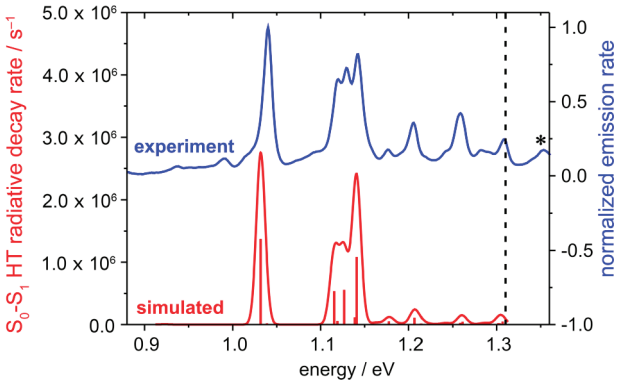

Figure 10. Emission spectra of ***c*-P6·T6**: experimental spectrum in methylcyclohexane at 78 K (excitation at 1.53 eV; 810 nm; blue line), Herzberg−Teller stick spectrum (red bars) and convoluted spectrum (red line, Gaussian σ = 5 meV). Convoluted-HT-spectrum peak heights are twice those of the stick spectrum as the e_1 HT modes occur in doubly degenerate pairs. The integrated HT radiative decay rate is 8.4 × 10^6 s^{-1}. The vertical dashed line marks the 0−0 transition energy at 1.31 eV (∗ indicates an impurity peak; see Supporting Information).

nonzero intensity for the combined vibronic HT transition. The intensity of the purely electronic state decreases proportionally to the intensity of the HT transition and the strength of this "intensity borrowing" depends on the energy spacing between the states. In a simpler but less informative picture of HT coupling, nuclear motions along non-totally-symmetric vibrational modes break the D_6 symmetry of the electronic wave function, resulting in a net transition dipole moment to the ground state.

The HT framework accounts for intensity borrowing via the first derivative of the transition dipole moment with respect to displacement of the nuclear coordinates along vibrational modes.[35] A detailed description of our model can be found in the Computational Methods section. We begin by calculating the vibrational modes of ***c*-P6·T6** at the DFT level using the BHLYP functional with the 6-31g(d,p) basis set. Comparing the simulated and experimental IR spectra shows that agreement is acceptable if the BHLYP frequencies are multiplied by a literature scaling factor of 0.940 (Figure 9).[37]

The normal modes plotted in Figure 9 were used to calculate S_0−S_1 transition dipole moment derivatives and resulting HT-induced transition intensities for all modes of e_1 symmetry, thus providing the vibronic envelope of the S_0−S_1 electronic transition. Accurate prediction of the 0−0 energy for a system of this size represents a formidable challenge. When the electronic transition energies were calculated using various computational methods, the energies were found to be method-dependent (see Supporting Information), thus we assumed an energy of 1.31 eV for the 0−0 transition by matching the simulated HT spectrum to the experimental low-temperature fluorescence spectrum (Figure 10). The simulated HT spectrum reproduces the vibronic structure of the low-temperature emission spectrum remarkably well considering the complexity of the system. Additionally, calculated radiative rate constants of the HT transitions are in good agreement with the experimentally determined values (see Supporting Information), confirming the accuracy of our predicted HT transition intensities. The small peak in the experimental fluorescence spectrum at 1.36 eV, which is at higher energy than the assumed S_0−S_1 0−0 of 1.31 eV, is attributed to a fluorescent impurity (see Supporting Information; this impurity is indicated by ∗ in Figures 7 and 10).

The most strongly coupled HT mode (mode 968) has a scaled frequency of 2244 cm^{-1} (278 meV) and corresponds to bond stretching in the butadiyne links, as represented schematically by the black arrows in Figure 8d−f. The vibration bisects the ring, creating two segments characterized by decreased and increased bond length alternation and thus increased and decreased conjugation, respectively. The change in bond length alternation is schematically represented by the bonds drawn around the distorted rings of Figure 8d−f. INDO/SCI atomic transition densities of the S_1, $S_2(x)$, and $S_2(y)$ electronic transitions at the reference D_6 ground state geometry and after a displacement of 0.053 Å (i.e., 0.1a_0, where a_0 is the Bohr radius) along mode 968 are also shown, providing a didactic visualization of the HT intensity-borrowing effect. The displacement disrupts the perfect symmetry of the S_0−S_1 atomic transition densities present in the D_6 geometry, resulting in a net transition dipole moment in the distorted structure. The increase in S_1 transition density for the more conjugated segment of the ring is accompanied by a decrease in $S_2(y)$ transition density in the same segment, since the S_0−S_1 transition borrows intensity from the S_0−$S_2(y)$ transition. This is confirmed by the decrease in $S_2(y)$ oscillator strength, which is approximately equal to the increase in S_0−S_1 oscillator strength. Modes of e_1 symmetry occur in pairs of doubly degenerate x and y polarized vibrations, which couple to the degenerate S_0−$S_2(x)$ and S_0−$S_2(y)$ electronic transitions, respectively. The other strongly HT coupled modes also have a butadiyne bond stretching component.

Having obtained a thorough understanding of the low-temperature fluorescence spectrum of ***c*-P6·T6**, which is due entirely to HT S_0−S_1 transitions, we turn our attention briefly to the absorption spectrum (Figure 7e). The theoretical analysis presented above indicates that the S_0−S_1 (0−0) absorption is an extremely weak band at about 945 nm. We believe the three main peaks in absorption are a result of coupling of the strongly allowed doubly degenerate x and y polarized S_2−S_0 electronic transition (Figure 8) to vibrational transitions. Whether the transitions are the result of a Franck−Condon vibronic progression that can be interpreted within an adiabatic Born−Oppenheimer framework (in which the dynamics of the electronic and nuclear degrees of freedom can be decoupled) or whether they are the result of dynamic vibronic coupling within a nonadiabatic framework is currently unclear. The fact that the three peaks have approximately equal spacings of 75 meV is compatible with a Franck−Condon

dx.doi.org/10.1021/ja2045919 |*J. Am. Chem. Soc.* 2011, 133, 17262–17273

interpretation. However, the importance of nonadiabatic coupling in systems featuring degenerate electronic states is well-known.[38] Work is in progress to investigate both possibilities.

Comparison of the calculated geometries of ***c*-P6** and ***c*-P6·T6** indicates that the N···N diameter of the **T6** template (20.06 Å) is about 0.5 Å less than the ideal size for binding ***c*-P6**. This confirms the conclusion from the crystal structure of ***c*-P6·T6** that the template is slightly too small for the cavity. Although the symmetry of the calculated gas-phase structure of ***c*-P6·T6** is different from that in the solid state, the calculated bond lengths and bond angles match well with the crystallographic values. For example calculations using the BHLYP functional gave a Zn···Zn diameter of 24.37 Å, which agrees with the crystallographic distance of 24.35 Å. Similarly the calculated value of $(\theta_1 + \theta_2)$ is 343.1°, which is close to the mean crystallographic value of 338.6° (Figure 5d).

CONCLUSIONS

The six-porphyrin nanoring ***c*-P6** can be synthesized in one step from porphyrin monomer ***l*-P1**, making it a readily available systems in which to explore the consequences of conjugation around a cylindrical barrel-shaped π-system. The free nanoring and its template complex ***c*-P6·T6** adopt essentially the same conformation in solution, as demonstrated by small-angle X-ray scattering (SAXS) measurements, although the ^{1}H NMR and UV−vis−NIR spectra show that the free nanoring is more flexible. The crystal structure of ***c*-P6·T6** reveals that most of the distortion in the nanoring is located in the acetylenic bridges. There is a slight bend in the porphyrin units, but the zinc coordination sphere is undistorted. The solid-state structure of ***c*-P6·T6** reveals a surprising ruffling of the whole nanoring, indicating that the template is slightly too small for the cavity of the macrocycle.

Ultrafast fluorescence anisotropy measurements show that absorption of light by ***c*-P6** and ***c*-P6·T6** generates excited states that are delocalized over the whole π-system. The optical absorption and fluorescence spectra exhibit remarkably complex patterns of sharp peaks. The fluorescence spectrum of ***c*-P6·T6** extends over a wide region of the near-infrared, from 900 to 1300 nm. These extraordinary spectra motivated the theoretical study presented above. Similar red-shifted fluorescence has been reported in cyclo[*n*]thiophenes,[28a] [*n*]paraphenylacetylenes[2a] and [*n*]cycloparaphenylenes,[3] but the effect is most pronounced in ***c*-P6·T6**.

The results of the quantum chemical DFT and INDO/SCI calculations presented here are significant for two reasons. First they show that the puzzling NIR fluorescence spectrum of ***c*-P6·T6** can be fully explained by vibronic Herzberg−Teller intensity borrowing from S_2 to S_1. Second, by providing an assignment for the fluorescence spectrum of ***c*-P6·T6**, they enable us to identify the S_0−S_1 0−0 transition (E_{00} = 1.31 eV). The corresponding S_0−S_1 gap for the free nanoring ***c*-P6** is E_{00} = 1.38 eV (measured in toluene with 1% pyridine). These optical gaps are lower than those of the corresponding linear hexamer (**Si$_2$-*l*-P′6**; E_{00} = 1.48 eV) or linear polymer (***l*-P′*N***; $N \approx$ 30−50; E_{00} = 1.46 eV), both measured in toluene with 1% pyridine. In low-viscosity solvents such as toluene, the excited states of linear porphyrin oligomers planarize prior to emission,[39] so the red-shifted emission of the nanoring is unlikely to be related to the distribution of porphyrin−porphyrin torsional angles. Comparison of the absorption and fluorescence spectra of ***c*-P6·T6** and **Si$_2$-*l*-P6·T6** indicates that the unique electronic structure of the nanoring results partly from bending of the π-system and partly from the high symmetry. Both the optical S_1−S_0 gap (E_{00} = 1.31 eV) and the electrochemical HOMO−LUMO gap (E_g = 1.55 V) of ***c*-P6·T6** are lower than those of the analogous linear oligomers. The difference between these two types of gap, which is the exciton binding energy ($E_{exc} = E_g - E_{00}$ = 0.24 eV), is slightly lower than that in linear porphyrin oligomers (e.g., E_{exc} = 0.29 eV for **Si$_2$-*l*-P4**).[24] The free nanoring ***c*-P6** has an identical exciton binding energy to ***c*-P6·T6**. It has been suggested, based on computational results, that the red-shifted fluorescence spectra of [*n*]cycloparaphenylenes originate from unusually high exciton binding energies,[3a,28b] but to the best of our knowledge, ***c*-P6** is the first conjugated belt-like macrocycle in which the exciton binding energy has been measured experimentally, by comparing electrochemical and optical gaps. We see no evidence for a high exciton binding energy in the nanoring.

Evidence for completed delocalization in the first excited state of ***c*-P6·T6** is provided by the small S_1−S_0 radiative rate constant, by the ultrafast fluorescence anisotropy depolarization, and by the excellent match between the calculated and observed fluorescence spectra (Figure 10). Our theoretical analysis indicates that the nonemissive S_1 state of ***c*-P6·T6** is fully delocalized over all six porphyrins (Figure 8a), whereas the strongly allowed S_2 state is delocalized over four of the six porphyrins (Figure 8b,c). HT coupling between these two states gives rise to the observed fluorescence spectrum. If the S_1 state were to self-localize onto a few adjacent porphyrin units, then the S_1−S_0 transitions would become strongly allowed and would dwarf any HT transitions. The very weak purely electronic 0−0 transition (at 946 nm) is a clear signature of a fully delocalized lowest excited state. The multiple satellites in the fluorescence spectrum arise from dynamic HT coupling to vibrational modes, rather than from static distortions that would result in symmetry breaking and localization of excitation.

The results presented here give a coherent picture of the electronic structure of a π-conjugated nanoring with a diameter of 2.4 nm. They show that this six-porphyrin nanoring behaves as a single π-system, not as an assembly of six discrete porphyrin chromophores. It will be interesting to explore how the electronic structure evolves in the larger nanorings of this family[4] and how the unusual behavior of these materials can be exploited.[40,41]

METHODS AND MATERIALS

Synthetic Procedures. All precursors were prepared according to the literature references given in the main text (see Supporting Information for details).

Synthesis of *c*-P6·T6. Hexadentate template **T6** (100 mg, 0.100 mmol) and porphyrin monomer ***l*-P1** (370 mg, 0.463 mmol) were dissolved in $CHCl_3$ (500 mL) and sonicated for 30 min (bath sonicator). A catalyst solution was prepared by dissolving $Pd(PPh_3)_2Cl_2$ (108 mg, 0.154 mmol), copper(I) iodide (147 mg, 0.772 mmol), and 1,4-benzoquinone (334 mg, 3.09 mmol) in $CHCl_3$ (90 mL) and freshly distilled diisopropylamine (3.7 mL). The catalyst solution was added to the porphyrin solution, and the mixture was stirred at room temperature for 2 h, and then at 50 °C for 1 h (under air). The mixture was passed through a plug of alumina using $CHCl_3$ as eluent, and purified by size exclusion chromatography on Biobeads S-X1 in toluene. The second band was isolated and recrystallized by layer addition (CH_2Cl_2/MeOH) to give ***c*-P6·T6** as a dark brown solid (93 mg, 21%).

Solution Small-Angle X-ray Scattering. The synchrotron radiation SAXS data were collected using standard procedures on the

I22 beamline at Diamond Light Source (UK) equipped with a photon-counting detector. The beam was focused onto the detector placed at a distance of 1.25 m from the sample cell. The X-ray wavelength was $\lambda = 1.0$ Å, and scattering was recorded across the region $0.03 < q < 1.0$ Å^{-1}. The data were normalized to the intensity of the incident beam; the scattering of the solvent was subtracted using an in-house program. To check for radiation damage during the SAXS experiment, the data were collected in 10 successive 60 s frames. All SAXS measurements were performed in either toluene or toluene/1% pyridine at known concentrations ($\sim 10^{-4}$ M) in a solution cell with mica windows (1 mm path length). Simulated scattering curves from molecular models were obtained by fitting to the experimental scattering data using the program CRYSOL.[42] The program GNOM[43] was used to calculate pair distribution functions and radii of gyration from experimental and simulated scattering data.

X-ray scattering data were also recorded on a solution of ***c*-P6·T6** in toluene at beamline 12-ID-C, Advanced Photon Source, Argonne National Laboratory, Argonne, Illinois, USA, using samples in 2 mm quartz capillaries with a wall thickness of 0.2 mm. The instrument utilized a double-crystal Si(111) monochromator and a two-dimensional mosaic CCD detector. The X-ray wavelength was $\lambda = 1.0$ Å and the sample-to-detector distances were adjusted to record scattering across the regions $0.006 < q < 0.2$ Å^{-1} and $0.29 < q < 2.1$ Å^{-1}.

Crystallography. Single-crystal diffraction data for ***c*-P6·T6** were collected at low temperature[44] with synchrotron radiation using beamline I19 (EH1) at the Diamond Light Source. The data were collected and reduced using CrystalClear (Rigaku Inc., 2009). Initially, small black hexagonal plate-like crystals were attempted; these gave a hexagonal cell of $a = 49.85$ Å, $c = 29.46$ Å, $V = 63395$ Å^3 that ultimately did not solve (details are given in the CIF). Dark green plate-like crystals gave better data, and the structure was solved with SuperFlip[45] and was refined using full-matrix least-squares within CRYSTALS.[46] Same-distance restraints were necessary to maintain sensible geometries for the disordered components; positional parameters for the porphyrin cores and acetylene bridges were unrestrained; however, thermal restraints were necessary throughout. Standard uncertainties were calculated from the full-matrix least-squares, except where an average value is given and the sample standard deviation is used. The structure was compared with literature values taken from the Cambridge Structural Database (CSD Version 5.32 with Nov. 2010 update).[47] Crystallographic data for ***c*-P6·T6** (excluding structure factors) have been deposited with the Cambridge Crystallographic Data Centre and can be obtained via www.ccdc.cam.ac.uk/data_request/cif.

Electrochemistry. Electrochemical experiments were performed using an Autolab PGSTAT12 potentiostat. Compounds were dissolved in freshly distilled THF containing Bu_4NBF_4 (0.1 M), under helium. A 3 mm glassy carbon working electrode was used with a Pt wire counter electrode and a $Ag/AgNO_3$ reference electrode. The redox potentials of all the compounds synthesized during this study were measured using square-wave voltammetry; the reversibility of the redox waves was checked by cyclic voltammetry.

Computational Methods. HT spectra can be calculated at many levels of approximation, both in terms of the quantum chemical method used and assumptions made about the ground and excited state potential energy surfaces.[36] Here we adopt a similar approach to that found in ref 36d, which assumes the harmonic approximation, negligible normal mode rotation (Duschinsky effect) upon excitation, and identical frequencies in S_0 and S_1. We consider only 0−1 vibronic transitions (i.e., from the vibrational ground state of the electronic excited to the first vibrationally excited state of the electronic ground state). The 0−1 squared HT transition dipole moment $\mu_{HT,i}^2$ (to which the spectral intensity is proportional) for each mode i of e_1 symmetry having reduced mass m_i and frequency ω_i is calculated from the first derivative $\partial\mu/\partial Q_i$ of the S_0-S_1 transition dipole moment μ with respect to displacement Q_i along the mode

$$\mu_{HT,i}^2 = \left[\left(\frac{\partial\mu}{\partial Q_i}\right)\langle 1_i|\hat{Q}_i|0_i\rangle\right]^2 = \left[\left(\frac{\partial\mu}{\partial Q_i}\right)\sqrt{\frac{\hbar}{2m_i\omega_i}}\right]^2 \quad (1)$$

The S_0-S_1 transition dipole moment derivative $\partial\mu/\partial Q_i$ of each of the 356 modes of e_1 symmetry was evaluated numerically by performing semiempirical INDO/SCI excited state calculations on geometries displaced 0.06 and $0.1a_0$ away from the ground state D_6 geometry along the normal coordinates of the mode. Both displacements yielded similar $\partial\mu/\partial Q_i$ derivatives (see Supporting Information) indicating the suitability of the linear HT approximation. Furthermore, the INDO/SCI results indicated that the HT spectrum was dominated by four sets of doubly degenerate e_1 modes. Numerical $\partial\mu/\partial Q_i$ derivative calculations were repeated at the higher TD-DFT level of theory for these modes, and the results were in good agreement with the INDO/SCI results (see Supporting Information). Geometry optimizations and normal mode calculations were performed using the BHLYP (50% of Hartree−Fock exchange)[31] DFT functional with the 6-31g(d,p) basis set in Turbomole, v. 5.9.1.[48] The m5 numerical quadrature grid was used, and the SCF convergence criterion was set to 10^{-9}. During optimizations, symmetry was constrained to D_6. The absence of imaginary frequencies indicated the presence of a true minimum in the D_6 potential energy surface. INDO/SCI[37] calculations were performed using in-house software. The active space comprised the first 120 occupied and virtual orbitals for which the properties of the S_0-S_1 and S_0-S_2 transitions were deemed to have converged. TD-DFT calculations were performed at the BHLYP 6-31g(d,p) level using Gaussian 09.[49]

■ ASSOCIATED CONTENT

Supporting Information. Synthetic procedures, characterization data, and computational details. This material is available free of charge via the Internet at http://pubs.acs.org.

■ AUTHOR INFORMATION

Corresponding Author
harry.anderson@chem.ox.ac.uk; david.beljonne@umons.ac.be

■ ACKNOWLEDGMENT

We thank the following organizations for support: the European Commission (through THREADMILL, MRTN-CT-2006-036040, and ONE-P, NMP3-LA-2008-212311), the Interuniversity Attraction Pole program of the Belgian Federal Science Policy Office (PAI 6/27), Programme d'Excellence de la Région Wallonne (OPTI2MAT project), FNRS-FRFC, the Swedish Energy Agency, the Clarendon Fund (D.V.K.), and the Chemical Sciences, Geosciences, and Biosciences Division, Office of Basic Energy Sciences, DOE under Grant No. DE-FG02-99ER14999. Prof. R. J. Nicholas provided valuable access to NIR emission instrumentation and M. C. O'Sullivan helped with part of the synthesis. We thank the EPSRC Mass Spectrometry Service (Swansea) for mass spectra. Use of the Advanced Photon Source at Argonne National Laboratory was supported by the U. S. Department of Energy, Office of Science, Office of Basic Energy Sciences, under Contract No. DE-AC02-06CH11357. D. B. is a FNRS Research Director. We thank Diamond Light Source for an award of beamtime on I19 (MT1858) and I22, and the instrument scientists (Dr. K. E. Christensen and Dr. D. R. Allan) for support.

REFERENCES

(1) (a) Krömer, J.; Rios-Carreras, I.; Fuhrmann, G.; Musch, C.; Wunderlin, M.; Debaerdemaeker, T.; Mena-Osteritz, E.; Bäuerle, P. *Angew. Chem., Int. Ed.* **2000**, *39*, 3481–3486. (b) Zhang, F.; Götz, G.; Winkler, H. D. F.; Schalley, C. A.; Bäuerle, P. *Angew. Chem., Int. Ed.* **2009**, *48*, 6632–6635. (c) Mayor, M.; Dischdies, C. *Angew. Chem., Int. Ed.* **2003**, *42*, 3176–3179. (d) Nakao, K.; Nishimura, M.; Tamachi, T.; Kuwatami, Y.; Miyasaka, H.; Nishinaga, T.; Iyoda, M. *J. Am. Chem. Soc.* **2006**, *128*, 16740–16747.

(2) (a) Kawase, T.; Darabi, H. R.; Oda, M. *Angew. Chem., Int. Ed. Engl.* **1996**, *35*, 2664–2666. (b) Ohkita, M.; Ando, K. R.; Tsuji, T. *Chem. Commun.* **2001**, 2570–2571.

(3) (a) Jasti, R.; Bhattacharjee, J.; Neaton, J. B.; Bertozzi, C. R. *J. Am. Chem. Soc.* **2008**, *130*, 17646–17647. (b) Yamago, S.; Watanabe, Y.; Iwamoto, T. *Angew. Chem., Int. Ed.* **2010**, *49*, 757–759. (c) Omachi, H.; Matsuura, S.; Segawa, Y.; Itami, K. *Angew. Chem., Int. Ed.* **2010**, *49*, 10202–10205. (d) Iwamoto, T.; Watanabe, Y.; Sakamoto, Y.; Suzuki, T.; Yamago, S. *J. Am. Chem. Soc.* **2011**, *133*, 8354–8361. (f) Sisto, T. J.; Golder, M. R.; Hirst, E. S.; Jasti, R. *J. Am. Chem. Soc.* **2011**, *133*, 15800–15802.

(4) (a) Hoffmann, M.; Wilson, C. J.; Odell, B.; Anderson, H. L. *Angew. Chem., Int. Ed.* **2007**, *46*, 3122–3125. (b) Hoffmann, M.; Kärnbratt, J.; Chang, M.-H.; Herz, L. M.; Albinsson, B.; Anderson, H. L. *Angew. Chem., Int. Ed.* **2008**, *47*, 4993–4996. (c) O'Sullivan, M. C.; Sprafke, J. K.; Kondratuk, D. V.; Rinfray, C.; Claridge, T. D. W.; Saywell, A.; Blunt, M. O.; O'Shea, J. N.; Beton, P. H.; Malfois, M.; Anderson, H. L. *Nature* **2011**, *469*, 72–75.

(5) (a) Bhaskar, A.; Ramakrishna, G.; Hagedorn, K.; Varnavski, O.; Mena-Osteritz, E.; Bäuerle, P.; Goodson, T., III *J. Phys. Chem. B* **2007**, *111*, 946–954. (b) Williams-Harry, M.; Bhaskar, A.; Ramakrishna, G.; Goodson, T., III; Imamura, M.; Mawatari, A.; Nakao, K.; Enozawa, H.; Nishinaga, T.; Iyoda, M. *J. Am. Chem. Soc.* **2008**, *130*, 3252–3253.

(6) (a) Kawase, T.; Tanaka, K.; Shiono, N.; Seirai, Y.; Oda, M. *Angew. Chem., Int. Ed.* **2004**, *43*, 1722–1724. (b) Kawase, T.; Nishiyama, Y.; Nakamura, T.; Ebi, T.; Matsumoto, K.; Kurata, H.; Oda, M. *Angew. Chem., Int. Ed.* **2007**, *46*, 1086–1088. (c) Mena-Osteritz, E.; Bäuerle, P. *Adv. Mater.* **2006**, *18*, 447–451. (d) Schmaltz, B.; Rouhanipour, A.; Räder, H. J.; Pisula, W.; Müllen, K. *Angew. Chem., Int. Ed.* **2009**, *48*, 720–724. (e) Pan, G.-P.; Cheng, X.-H.; Höger, S. *J. Am. Chem. Soc.* **2006**, *128*, 4218–4219. (f) Chen, T.; Pan, G.-B.; Wettach, H.; Fritzsche, M.; Höger, S.; Wan, L.-J.; Yang, H.-B.; Northrop, B. H.; Stang, P. J. *J. Am. Chem. Soc.* **2010**, *132*, 1328–1333.

(7) Zhang, W.; Moore, J. S. *Angew. Chem., Int. Ed.* **2006**, *45*, 4416–4439.

(8) (a) Kawase, T.; Kurata, H. *Chem. Rev.* **2006**, *106*, 5250–5273. (b) Tahara, K; Tobe, Y. *Chem. Rev.* **2006**, *106*, 5274–5290.

(9) (a) Jung, S.-H.; Pisula, W.; Rouhanipour, A.; Räder, H. J.; Jacob, J.; Müllen, K. *Angew. Chem., Int. Ed.* **2006**, *45*, 4685–4690. (b) Mössinger, D.; Hornung, J.; Lei, S.; De Feyter, S.; Höger, S. *Angew. Chem., Int. Ed.* **2007**, *46*, 6802–6806.

(10) (a) Anderson, S.; Anderson, H. L.; Sanders, J. K. M. *Acc. Chem. Res.* **1993**, *26*, 469–475. (b) Anderson, S.; Anderson, H. L.; Sanders, J. K. M. *J. Chem. Soc., Perkin Trans. 1* **1995**, 2255–2267. (c) McCallien, D. W.; Sanders, J. K. M. *J. Am. Chem. Soc.* **1995**, *117*, 6611–6612.

(11) Lovett, J. E.; Hoffmann, M.; Cnossen, A.; Shutter, A. T. J.; Hogben, H. J.; Warren, J. E.; Pascu, S. I.; Kay, C. W. M.; Timmel, C. R.; Anderson, H. L. *J. Am. Chem. Soc.* **2009**, *131*, 13852–13859.

(12) Cyclic porphyrin oligomers are substantially more soluble than their linear counterparts. In this work, we used octyloxy side chains to solubilize the linear oligomers, whereas the cyclic hexamer is sufficiently soluble with *tert*-butyl substituents. The change from OC_8H_{17} to *t*-Bu *meta*-aryl substituents has a negligible effect on the electronic structure of the porphyrin oligomer π-system.

(13) Liu, Q.; Burton, D. J. *Tetrahedron Lett.* **1997**, *38*, 4371–4374.

(14) Williams, V. E.; Swager, T. M. *J. Polym. Sci., Part A: Polym. Chem.* **2000**, *38*, 4669–4676.

(15) (a) Newman, M. S.; Lee, L. F. *J. Org. Chem.* **1972**, *37*, 4468–4469. (b) Littler, B. J.; Miller, M. A.; Hung, C.-H.; Wagner, R. W.; O'Shea, D. F.; Boyle, P. D.; Lindsey, J. S. *J. Org. Chem.* **1999**, *64*, 1391–1396.

(16) (a) Taylor, P. N.; Anderson, H. L. *J. Am. Chem. Soc.* **1999**, *121*, 11538–11545. (b) Plater, M. J.; Aiken, S.; Bourhill, G. *Tetrahedron* **2002**, *58*, 2405–2413.

(17) (a) Svergun, D. I.; Koch, M. H. J. *Rep. Prog. Phys.* **2003**, *66*, 1735–1782. (b) Putnam, C. D.; Hammel, M.; Hura, G. L.; Tainer, J. A. *Q. Rev. Biophys.* **2007**, *40*, 191–285.

(18) (a) Tiede, D. M.; Zhang, R.; Chen, L. X.; Yu, L.; Lindsey, J. S. *J. Am. Chem. Soc.* **2004**, *126*, 14054–14062. (b) Sinks, L. E.; Rybtchinski, B.; Iimura, M.; Jones, B. A.; Goshe, A. J.; Zuo, X.; Tiede, D. M.; Li, X.; Wasielewski, M. R. *Chem. Mater.* **2005**, *17*, 6295–6303. (c) Wasielewski, M. R. *Acc. Chem. Res.* **2009**, *42*, 1910–1921.

(19) Song, J.; Aratani, N.; Kim, P.; Kim, D.; Shinokubo, H.; Osuka, A. *Angew. Chem., Int. Ed.* **2010**, *49*, 3617–3620.

(20) Taylor, P. N.; Huuskonen, J.; Rumbles, G.; Aplin, R. T.; Williams, E.; Anderson, H. L. *Chem. Commun.* **1998**, 909–910.

(21) Song, J.; Aratani, N.; Shinokubo, H.; Osuka, A. *J. Am. Chem. Soc.* **2010**, *132*, 16356–16357.

(22) (a) Eisler, S.; McDonald, R.; Loppnow, G. R.; Tykwinski, R. R. *J. Am. Chem. Soc.* **2000**, *122*, 6917–6928. (b) Collins, S. K.; Yap, G. P. A.; Fallis, A. G. *Angew. Chem., Int. Ed.* **2000**, *39*, 385–388. (c) Zhang, L; Gopee, H.; Hughes, D. L.; Cammidge, A. N. *Chem. Commun.* **2010**, *46*, 4255–4257. (d) Mitzel, F.; Boudon, C.; Gisselbrecht, J.-P.; Seiler, P.; Gross, M.; Diederich, F. *Chem. Commun.* **2003**, 1634–1635. (e) Ojima, J.; Hiraiwa, N.; Higuchi, H.; Kobayashi, I.; Yamamoto, K.; Yoshida, T.; Adachi, T.; Matsubara, H.; Yamamoto, G. *J. Chem. Soc., Perkin Trans. 1* **1996**, 2755–2763. (f) Yamamoto, G.; Mazaki, Y.; Kobayashi, R.; Higuchi, H.; Ojima, J. *J. Chem. Soc., Perkin Trans. 1* **1997**, 3183–3188.

(23) Chalifoux, W. A.; McDonald, R.; Ferguson, M. J.; Tykwinski, R. R. *Angew. Chem., Int. Ed.* **2009**, *48*, 7915–7919.

(24) Winters, M. U.; Dahlstedt, E.; Blades, H. E.; Wilson, C. J.; Frampton, M. J.; Anderson, H. L.; Albinsson, B. *J. Am. Chem. Soc.* **2007**, *129*, 4291–4297.

(25) The fluorescence spectra of ***c*-P6** and ***c*-P6·T6** shown in Figure 7 are very different from those reported in ref 4b because the earlier spectra were recorded on a fluorimeter with poor sensitivity at wavelengths greater than 950 nm.

(26) Fluorescence decay times for ***c*-P6·T6** and **Si_2-*l*-P′6** were presented in ref 4b; however there was an error in the value reported for ***c*-P6·T6** (probably due to traces of fluorescent impurities). Repeated measurements on highly purified samples of ***c*-P6·T6** (detecting emission at 850, 914, 950, and 980 nm) reproducibly give $\tau_F = 250 \pm 10$ ps; see Supporting Information.

(27) Chang, M.-H.; Hoffmann, M.; Anderson, H. L.; Herz, L. M. *J. Am. Chem. Soc.* **2008**, *130*, 10171–10178.

(28) (a) Bednarz, M; Reineker, P.; Mena-Osteritz, E.; Bäuerle, P. *J. Lumin.* **2004**, *110*, 225–231. (b) Wong, B. M. *J. Phys. Chem. C* **2009**, *113*, 21921–21927. (c) Sundholm, D.; Taubert, S.; Pichierri, F. *Phys. Chem. Chem. Phys.* **2010**, *12*, 2751–2757.

(29) Ridley, J.; Zerner, M. C. *Theor. Chim. Acta* **1973**, *32*, 111–134.

(30) Marques, M. A. L.; Gross, E. K. U. *Annu. Rev. Phys. Chem.* **2004**, *55*, 427–455.

(31) Becke, A. D. *J. Chem. Phys.* **1993**, *98*, 1372–1378.

(32) (a) The electric dipole (ED) operator transforms as $A_{2u}(z) + E_{1u}(x,y)$ in D_{6h}. Thus the bra-ket expansion $\langle\psi(S_0)|\mu|\psi(S_1)\rangle = \langle A_{1g}|A_{2u} + E_{1u}|A_{2g}\rangle = \langle A_{1g}|A_{2u}|A_{2g}\rangle + \langle A_{1g}|E_{1u}|A_{2g}\rangle = \langle A_{1g}|A_{1u}\rangle + \langle A_{1g}|E_{1u}\rangle$ and is therefore forbidden. (b) The bra-ket expansion $\langle\psi(S_0)|\mu|\psi(S_2)\rangle = \langle A_{1g}|A_{2u} + E_{1u}|E_{1u}\rangle = \langle A_{1g}|A_{2u}|E_{1u}\rangle + \langle A_{1g}|E_{1u}|E_{1u}\rangle = \langle A_{1g}|E_{1g}\rangle + \langle A_{1g}|A_{1g} + A_{2g} + E_{2g}\rangle$ and is therefore allowed via $E_{1u}(x,y)$. (c) The bra-ket expansion $\langle\psi(S_0)|\mu|\psi(S_1)\rangle = \langle A_{1g}|A_{2u} + E_{1u}|B_{2u}\rangle = \langle A_{1g}|A_{2u}|B_{2u}\rangle + \langle A_{1g}|E_{1u}|B_{2u}\rangle = \langle A_{1g}|B_{1g}\rangle + \langle A_{1g}|E_{2g}\rangle$ and is therefore forbidden. (d) The electric dipole operator transforms as $A_2(z)+E_1(x,y)$ in D_6. Thus the bra-ket expansion $\langle\psi(S_0)|\mu|\psi(\mathrm{Vib}) \times \psi(S_1)\rangle = \langle A_1|A_2 + E_1|e_1 \times A_2\rangle = \langle A_1|A_2 + E_1|E_1\rangle = \langle A_1|A_2|E_1\rangle + \langle A_1|E_1|E_1\rangle = \langle A_1|E_1\rangle + \langle A_1|A_1 + A_2 + E_2\rangle$ and is therefore strongly allowed via $E_1(x,y)$.

(33) Hashimoto, T.; Nakano, H.; Hirao, K. *J. Mol. Struct.: THEOCHEM* **1998**, *451*, 25–33.

(34) Hiraya, A.; Shobatake, K. *J. Chem. Phys.* **1991**, *94*, 7700–7706.
(35) Herzberg, G.; Teller, E. *Z. Phys. Chem., Abt. B* **1933**, *21*, 410.
(36) (a) Bernhardsson, A.; Forsberg, N.; Malmqvist, P.; Roos, B. O.; Serrano-Andrés, L. *J. Chem. Phys.* **2000**, *112*, 2798–2809. (b) Niu, Y.; Peng, Q.; Deng, D.; Gao, X.; Shuai, Z. *J. Phys. Chem. A* **2010**, *114*, 7817–7831. (c) Santoro, F.; Lami, A; Improta, R.; Bloino, J.; Barone, V. *J. Chem. Phys.* **2008**, *128*, No. 224311. (d) Di Donato, E.; Vanzo, D.; Semeraro, M.; Credi, A.; Negri, F. *J. Phys. Chem. A* **2009**, *113*, 6504–6510.
(37) Merrick, J. P.; Moran, D.; Radom, L. *J. Phys. Chem. A* **2007**, *111*, 11683–11700.
(38) (a) Mahapatra, S. *Acc. Chem. Res.* **2009**, *42*, 1004–1015. (b) Bersuker, I. B. *Chem. Rev.* **2001**, *101*, 1067–1114.
(39) Winters, M. U.; Kärnbratt, J.; Eng, M.; Wilson, C. J.; Anderson, H. L.; Albinsson, B. *J. Phys. Chem. C* **2007**, *111*, 7192–7199.
(40) Fenwick, O.; Sprafke, J. K.; Binas, J.; Kondratuk, D. V.; Di Stasio, F.; Anderson, H. L.; Cacialli, F. *Nano Lett.* **2011**, *11*, 2451–2456.
(41) Raymond, J. E.; Bhaskar, A.; Goodson, T., III; Makiuchi, N.; Ogawa, K.; Kobuke, Y. *J. Am. Chem. Soc.* **2008**, *130*, 17212–17213.
(42) Svergun, D. I.; Berbato, C.; Koch, M. H. J. *J. Appl. Crystallogr.* **1995**, *28*, 768–773.
(43) Svergun, D. I. *J. Appl. Crystallogr.* **1992**, *25*, 495–503.
(44) Cosier, J.; Glazer, A. M. *J. Appl. Crystallogr.* **1986**, *19*, 105–107.
(45) Palatinus, L.; Chapuis, G. *J. Appl. Crystallogr.* **2007**, *40*, 786–790.
(46) (a) Betteridge, P. W.; Carruthers, J. R.; Cooper, R. I.; Prout, K.; Watkin, D. J. *J. Appl. Crystallogr.* **2003**, *36*, 1487. (b) Cooper, R. I.; Thompson, A. L.; Watkin, D. J. *J. Appl. Crystallogr.* **2010**, *43*, 1100–1107. (c) Watkin, D. J. *Acta Crystallogr.* **1994**, *A50*, 411–437. (d) Prince, E. *Mathematical Techniques in Crystallography and Materials Science*; Springer-Verlag: New York, 1982.
(47) (a) Allen, F. H. *Acta Crystallogr.* **2002**, *B58*, 380–388. (b) Bruno, I. J.; Cole, J. C.; Edgington, P. R.; Kessler, M.; Macrae, C. F.; McCabe, P.; Pearson, J.; Taylor, R. *Acta Crystallogr.* **2002**, *B58*, 389–397.
(48) Ahlrichs, R.; Bär, M.; Häser, M.; Horn, H.; Kölmel, C. *Chem. Phys. Lett.* **1989**, *162*, 165–169.
(49) Frisch, M. J. et al. *Gaussian 09*, Revision A.02, Gaussian, Inc.: Wallingford CT, 2009.